

NURBS-DIFF: A DIFFERENTIABLE NURBS LAYER FOR MACHINE LEARNING CAD APPLICATIONS

Anjana Deva Prasad¹, Aditya Balu¹, Harshil Shah¹, Soumik Sarkar¹, Adarsh Krishnamurthy^{1*}

¹ Iowa State University

Abstract

Recent deep-learning-based techniques for the reconstruction of geometries from different input representations such as images and point clouds have been instrumental in advancing research in geometric machine learning. Most of these techniques rely on a triangular mesh representation for representing the geometry, with very recent attempts in using B-splines. While Non-Uniform Rational B-splines (NURBS) are the de facto standard in the CAD industry, minimal efforts have been made to bridge the gap between deep-learning frameworks and the NURBS representation for geometry. The backbone of modern deep learning techniques is the use of a fully automatic differentiable definition for each mathematical operation to enable backpropagation of losses while training. In order to integrate the NURBS representation of CAD models with deep learning methods, we propose a differentiable NURBS layer for evaluating the curve or surface given a set of NURBS parameters. We have developed a NURBS layer defining the forward and backward pass required for automatic differentiation. Our implementation is GPU accelerated and is directly integrated with PyTorch, a popular deep learning framework. We demonstrate the efficacy of our NURBS layer by automatically incorporating it with the stochastic gradient descent algorithm and performing CAD operations such as curve or surface fitting and surface offsetting. Further, we show its utility in deep learning applications such as point cloud reconstruction and structural modeling and analysis of shell structures such as heart valves. These examples show that our layer has better performance for certain deep learning frameworks and can be directly integrated with any CAD deep-learning framework that require the use of NURBS.

Keywords

Differentiable NURBS Layer | NURBS | Geometric Deep Learning | Surface Modeling

1 Introduction

Deep Learning for 3D Euclidean geometry is emerging as a critical and well-explored research area in engineering. This area includes fundamental computer vision works such as 3D shape reconstructions from point clouds or multi-view stereo and 3D semantic segmentation for shape understanding^{3,11,15,18,42,47,50,52}. The common goal in these approaches is to obtain a consistent representation of the geometry by employing deep learning on the data acquired from different 3D sources or photogrammetric techniques. A prevalent challenge in all these efforts is to identify an ideal representation of the 3D geometry, such that it represents complex geometric information, encapsulates both local and global information, and has a compact representation that is tractable in terms of memory and computation. Often, triangular mesh representation is used for these applications due to their ubiquity in graphics²⁵. Concurrently, there is a separate research thrust that focuses on converting standard CAD representations to geometric representations that are more amenable to machine learning (such as voxels, triangular meshes, etc.)⁶. This conversion from the standard CAD geometries to other representations is often irreversible and is not trivial to incorporate in current deep learning approaches. This transformation from CAD geometries to learning-amenable representations creates a critical gap between these two concurrent research thrusts, not allowing for proper feedback or constraints between the CAD geometry and the 3D deep learning frameworks.

In modern CAD systems, a solid model is represented using boundary representation (B-Rep), where the solid boundaries are defined using spline surfaces. Non-Uniform Rational B-splines (NURBS) are the standard representation used for defining the spline surfaces⁵³. NURBS surfaces offer a high level of control and versatility; they can also compactly represent the surface geometry. NURBS surfaces can represent more complex shapes than Bézier or B-splines due to the non-uniformity of the knot vectors and the non-linear transformation due to the weights assigned to the control points. In addition, the NURBS definition allows for local control via the knots and the control points and global control via the weights. While NURBS are the standard CAD representation in engineering, their utility in deep learning-based approaches is not

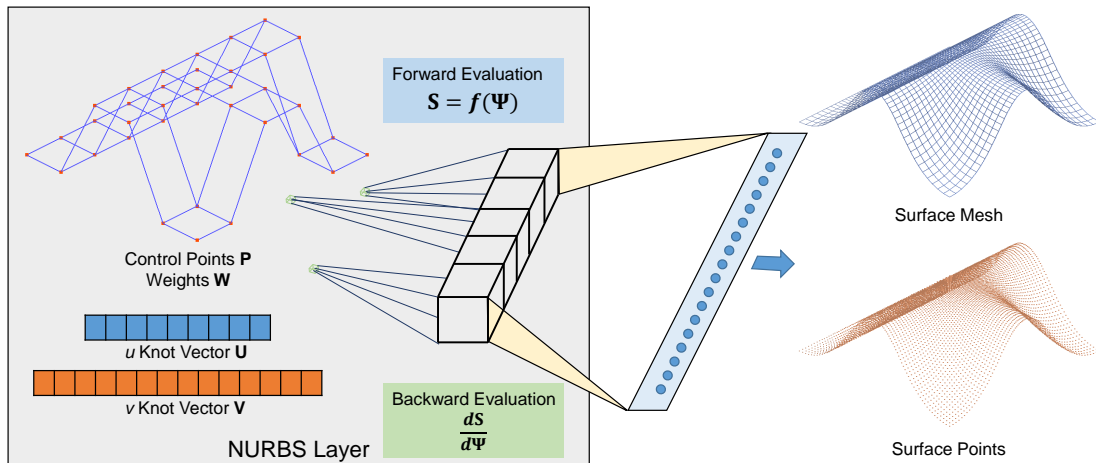


Figure 1: We propose a differentiable NURBS layer for standard deep learning systems to enable them to predict standard CAD geometry *as-is* for applying geometric constraints. The NURBS parameters are input to the layer during the forward evaluation, and we evaluate the surface mesh. Once a loss is computed, and gradients for the surface mesh are obtained, we perform a backward evaluation to enable backpropagation through deep learning architectures.

well researched. One of the main challenges in extending NURBS-based representation to deep learning is the requirement for differentiable programming of the operations performed during neural network computations. This requires the complete mathematical definition of both the forward computations and the derivatives with respect to the input for the backward computations.

The main idea of differentiable programming is to leverage gradient-based approaches to optimize the input parameters to obtain a specific target output, allowing for end-to-end trainable systems (particularly useful in deep neural networks). This approach has found use in a large variety of applications such as scientific computing^{26,27,57}, image processing³⁶, physics engines¹⁶, computational simulations¹, and graphics^{10,35}. For differentiable programming of NURBS, we need to compute gradients of the NURBS surface points with respect to the parameters of the NURBS representation. However, since the NURBS surface points are a function of knots, control points, and weights, the partial derivative with respect to each input parameter needs to be computed, which makes the backward evaluation challenging. Further, due to the use of basis functions (which are piecewise-continuous polynomials), the gradients might be discontinuous (or even zero) at certain locations. To alleviate this issue, we exploit the recent theoretical advances in the paradigm of differentiable programming. It has been theoretically proven that if a weak form of the Jacobian for the “forward” evaluation operator can be represented using a *block-sparse* matrix, then this approximate Jacobian can be used for performing the “backward” evaluation of that operation^{12,14}. This approach has been used to define approximate derivatives for operations such as sorting^{8,14}, loops and algorithmic conditions, and even derivatives for piecewise polynomial functions⁷. We use a similar approach by defining a *block-sparse* Jacobian for NURBS surface representation and evaluation.

Formally, using the differentiable programming approach explained above, we formulate a differentiable NURBS “layer” (in deep learning terminology), which enables deep learning frameworks to integrate NURBS-based representation of B-Rep surfaces and perform CAD operations using them. The forward pass of our NURBS layer uses the standard NURBS evaluation as explained in Section 3.1. The backward pass uses the derivatives of the NURBS curve or surface with respect to the input parameters of the NURBS (Section 3.2). The derivatives are used to define the Jacobian that is then used for backpropagation of the losses during training. After defining the NURBS layer, we demonstrate its utility in performing traditional CAD operations such as curve fitting, surface fitting, and surface offsetting. We demonstrate that these operations can be performed using the gradient-based optimization techniques traditionally used in machine learning frameworks. Finally, we show the applicability of our NURBS layer in deep learning by using it as an additional decoder for point cloud reconstruction and for enforcing constraints in isogeometric finite element analysis of shell structures.

In this paper, we have developed a differential NURBS layer that can be used in machine learning and CAD applications. The key contributions of this work are:

1. A differentiable programming framework using NURBS representation. We redefine the NURBS operations such that they can be back-propagated. Specifically, we define the Jacobian based on the derivatives of the NURBS with respect to its input parameters.
2. A GPU-accelerated implementation of our NURBS layer in PyTorch for better integration with existing deep learning programming frameworks.
3. A gradient descent-based optimization framework using our differentiable NURBS layer for performing CAD operations such as curve fitting, surface fitting, and surface offsetting.
4. The applicability of our proposed differentiable programming framework to extend the training process of point cloud reconstruction to NURBS surfaces and add constraints on the geometry for deformation analysis.

The rest of the paper is arranged as follows. We outline some close related work in point cloud reconstruction, machine learning approaches in CAD, and differentiable programming in [Section 2](#). We provide the mathematical details of our differentiable NURBS layer in [Section 3](#). We show the application of the NURBS layer to CAD operations in [Section 4](#) and to deep learning [Section 5](#).

2 Related Work

The problem of extracting concise representations of geometry from a spectrum of input data formats such as images, depth maps, and point clouds has been extensively studied over the last few decades. While methodologies that derive such representations are pervasive in 3D reconstruction literature today, Our NURBS layer focuses on filling the gap between the NURBS-based CAD representation and the other input data format. In this context, we broadly categorize the prior related work under several sections, which illustrate several cross intersecting works with our present work.

2.1 Methods for 3D Reconstruction

We first discuss several supervised and unsupervised learning frameworks that use different object representations for 3D reconstruction (see [Figure 2](#)). Methods that perform point cloud reconstruction require understanding of both the global geometric structure and local features embedded near each point. Several such frameworks either operate directly on the point cloud or transform the point cloud to intermediate representations that can later be converted to standard formats used in CAD systems today. For the former, several works use hierarchical feature learning^{54,62}, upsampling,^{69,71} and graph convolutions^{45,69} to reason the geometry and underlying local and global features from the data. Despite the state-of-the-art results achieved through such techniques, the learned representations are not readily available for rendering and manufacturing applications. Among classes that learn intermediate representations, volumetric and mesh-based frameworks are popular. For volumetric techniques, different architectures that generate voxel^{65,70} and octree-based^{64,68} representations have been proposed that operate on a broad spectrum of input formats like single images, multi-view images^{13,29} and 3D voxel grids²⁴. Alternatively, methods that generate a collection of mesh patches from input point sets have also been proposed that overcome the low-resolution outputs that plagued point cloud and volumetric approaches²⁵. Another idea is to use implicit approaches for representing the geometry^{3,50}. However, for integrating our layer with 3D reconstruction frameworks, we focus on more recent works that directly learn a collection of parametric primitives^{34,59,60} from input point clouds. These approaches integrate well with current CAD systems that make use of parametric geometry. In our application, we generalize the B-spline and basic primitives generated from Sharma et al.⁶⁰ to include rational B-splines and NURBS surfaces.

2.2 Fitting CAD Primitives

The foundations of curve and surface fitting were built upon algorithms such as RANSAC, Hough Transforms, and Clustering.³¹ Improvements to the original RANSAC algorithm were made by Schnabel et al.⁵⁸ who introduced an iterative method to fit shapes such as planes, spheres, and cylinders to point clouds. Further enhancements included introducing a regularization step³⁷ and the addition of orientation constraints⁶¹ to the input data. While RANSAC-based techniques pioneered geometric primitive fitting

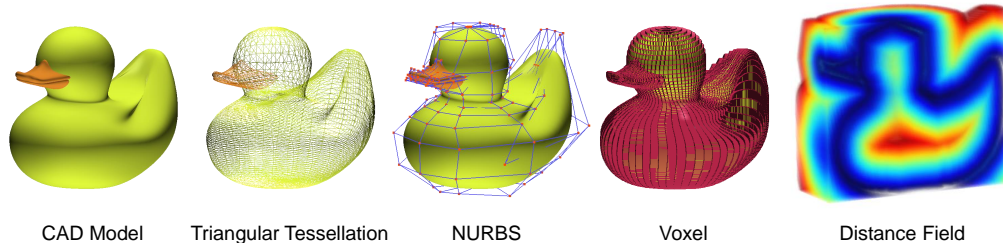


Figure 2: Different representations of the Ducky model used for deep learning applications. The NURBS surface provides the most compact representation.

at the time, they depended significantly on parameter tuning. Another popular method for primitive fitting, Hough transforms, used input space quantizations to decide the parameter sets that best represent the input²¹. Another popular early methodology used segmentation and clustering to identify geometric primitives. In clustering techniques,^{2,56} the points were aggregated into regions based on different heuristics related to the primitives. A well-established algorithm, the K-means clustering procedure⁴¹, computes k clusters from a spatial dataset by assigning points to their closest centers. In this paper, we use the stochastic gradient descent algorithm to fit NURBS curves and surfaces as explained in Section 4. Fitting NURBS surfaces for a set of point cloud is typically done by solving a set of equations as explained in Piegler and Tiller⁵³. Further, several iterative optimization based approaches have been established for performing the curve and surface fitting^{19,38,39,43,49}. To the best knowledge of the authors, there are no works where NURBS fitting is performed using state-of-the-art stochastic gradient descent based optimization.

2.3 Differentiable Programming

NURBS surfaces are obtained as a tensor product of two-piecewise polynomial B-spline curves. To conceptualize end-to-end trainable deep learning systems that can fit NURBS surfaces to various input geometries, we require a framework that can backpropagate over such piecewise polynomial functions. Several recent works have been proposed that take advantage of the differentiable programming paradigm to approximate gradients for such functions. Cuturi et al.¹⁴ and Blondel et al.⁹ propose differentiable operators for sorting based tasks. Similarly, Vlastelica et al.⁶⁷ compute gradients for several optimization problems by constructing linear approximations to discrete-values functions. We model our layer on prior work that incorporates structured priors as layers in the deep learning framework, similar to Sherifdeen et al.⁶³, Joshi et al.³⁰, and Djolonga and Krause²⁰. Beyond deep learning-based approaches, automatic differentiation for NURBS parametric coordinates for obtaining the surface derivatives for Adjoint-based sensitivity analysis has been performed by Zhang⁷². Ugolotti et al.⁶⁶ performed a gradient-based aerodynamic shape optimization using a robust Machine Learning model, which is created to integrate the geometry generation and the mesh generation process using one single polynomial layer for the volumetric mesh. Mykhaskiv et al.⁴⁶ define a differentiated CAD kernel in Open Cascade Technology for applying algorithmic differentiation to a complete CAD system for shape optimization and imposing constraints. These works encourage us to pursue this research work and present this robust NURBS layer for researchers to use in wide applications.

2.4 NURBS in Deep Learning

Several deep learning frameworks use NURBS. Minto et al.⁴⁴ uses NURBS surfaces fitted over the 3D geometry as an input representation for the object classification task of ModelNet10 and ModelNet40 datasets. Erwiniski et al.²² presented a neural-network-based contour error prediction method for NURBS paths. Fey et al.²³ presents a new convolution operator based on B-splines for irregular structured and geometric input, e.g., graphs or meshes. Balestrierio et al.⁴ build a theoretical link between deep networks and spline functions and build end-to-end deep learning systems using spline-based activation functions. Balu et al.⁵ propose a NURBS-aware convolutional neural network that maintains the topological structure in a similar way to a parametric NURBS surface evaluation grid. Very recently, Sharma et al.⁶⁰ perform point cloud reconstruction to predict a B-spline surface, which is later processed to obtain a complete CAD model with other primitives “stitched” together. In our work, we perform comparison between our approach and Balu et al.⁵ in Section 5.2. Similarly, we perform a comparison between our approach and Sharma et al.⁶⁰ in Section 5.1.

3 Differentiable NURBS Layer

Modern CAD systems make use of boundary-representation (B-Rep) for representing a solid geometry, Ω , which is embedded in a 2D or 3D Euclidean space (\mathbb{R}^2 or \mathbb{R}^3). A B-Rep consists of a set of surfaces $d\Omega$ representing the boundary of the solid. Each surface $\mathcal{S} \subset d\Omega$ in a standard CAD system is represented using a Non-Uniform Rational B-spline (NURBS) surface. The NURBS representation is a compact representation that uses a set of control points, knot vectors, degrees, and weights to map a parametric space to span the entire surface \mathcal{S} in the Euclidean space. In this work, we propose a differentiable NURBS “layer” which could evaluate the surface \mathcal{S} given the control points, knot vectors, degrees, and weights, usually obtained as an output from a deep learning system, $NN(\theta)$. This deep learning system is trained using a loss function $\mathcal{L}(\cdot, \cdot)$, computed between a target point cloud $\mathbf{P} \in \{\mathbb{R}^{N \times 2} \text{ or } \mathbb{R}^{N \times 3}\}$ (where N is the number of points) and a set of points \mathbf{S} sampled (or evaluated) from the surface \mathcal{S} . During the training process, the gradient of the loss function with respect to the parameters of the deep learning model, $\partial\mathcal{L}/\partial\theta$ is required for back propagation. It is usually straightforward to compute the derivative of the loss function $\partial\mathcal{L}/\partial\mathcal{S}$ for some of the standard loss functions used, such as Chamfer distance, L_2 distance, etc., since they are differentiable. However, $\partial\mathcal{L}/\partial\theta$ requires a mathematically consistent definition of $\partial\mathcal{S}/\partial\Psi$, where Ψ refers to the complete set of NURBS parameters (i.e. the set of control points \mathbf{P} , its corresponding weights \mathbf{W} , and the knot vectors \mathbf{U} and \mathbf{V}) that define the surface. The gradient $\partial\mathcal{S}/\partial\Psi$ is necessary because the deep learning system $NN(\theta)$ predicts this set of NURBS parameters Ψ and computing $\partial\mathcal{L}/\partial\theta$ requires computing $\partial\mathcal{S}/\partial\Psi$, $\partial\mathcal{L}/\partial\mathcal{S}$ and finally, $\partial\Psi/\partial\theta$. Formally, this can be explained using the chain rule as:

$$\frac{\partial\mathcal{L}}{\partial\theta} = \frac{\partial\mathcal{L}}{\partial\mathcal{S}} \frac{\partial\mathcal{S}}{\partial\Psi} \frac{\partial\Psi}{\partial\theta} \quad (1)$$

The main challenge in this approach is computing $\partial\mathcal{S}/\partial\Psi$. To this end, we propose a differentiable NURBS layer implemented as a forward and backward machine learning module. While our layer can handle both curve and surface point computations, we limit the discussions of our forward and backward algorithms to surfaces. As shown in the results section, the approach can be directly used for curves embedded in both 2D and 3D space by suitably adjusting the dimensions of the NURBS parameters.

3.1 Forward Evaluation for NURBS Surface

The NURBS surface \mathcal{S} is sampled over a finite parametric space (u, v) where $(u, v) \in ([0, 1] \times [0, 1])$, and this set of finite points \mathbf{S} representing the surface is used for performing the loss computation and the backward gradient computation. This set \mathbf{S} is computed as a function of NURBS parameters $\Psi = \{\mathbf{P}, \mathbf{U}, \mathbf{V}, \mathbf{W}\}$. Given the NURBS surface points are a function of the NURBS parameters in [Equation 2](#), we compute the forward evaluation using the NURBS formulation.

$$\mathbf{S} = \mathbf{f}(\mathbf{P}, \mathbf{U}, \mathbf{V}, \mathbf{W}) \quad (2)$$

3.1.1 NURBS Formulation

Formally, a point in the NURBS surface parametrized using (u, v) is defined as follows:

$$\mathbf{S}(u, v) = \frac{\sum_{i=0}^n \sum_{j=0}^m N_i^p(u) N_j^q(v) w_{ij} \mathbf{P}_{ij}}{\sum_{j=0}^m N_i^p(u) N_j^q(v) w_{ij}}, \quad (3)$$

Here, the basis functions of NURBS, (N_i, N_j) are polynomials that are recursively computed using Cox-de Boor recursion formula in [Equation 4](#), where u is the parameter value, N_i^p is the i^{th} basis function of degree p .

$$N_i^p(u) = \frac{u - u_i}{u_{i+p} - u_i} N_i^{p-1}(u) + \frac{u_{i+p+1} - u}{u_{i+p+1} - u_{i+1}} N_{i+1}^{p-1}(u) \quad (4)$$

$$N_i^0(u) = \begin{cases} 1 & \text{if } u_i \leq u \leq u_{i+1} \\ 0 & \text{otherwise} \end{cases} \quad (5)$$

Algorithm 1: Forward algorithm for multiple surfaces

Input : $\mathbf{U}, \mathbf{V}, \mathbf{P}, \mathbf{W}$, output resolution n_{grid}, m_{grid} **Output:** \mathbf{S} Initialize a meshgrid of parametric coordinates uniformly from $[0, 1]$ using $n_{grid} \times m_{grid} : u_{grid} \times v_{grid}$ Initialize: $\mathbf{S} \rightarrow \mathbf{0}$ **for** $k = 1 : \text{surfaces in parallel do}$ **for** $j = 1 : m_{grid} \text{ points in parallel do}$ **for** $i = 1 : n_{grid} \text{ points in parallel do}$ Compute u_{span} and v_{span} for the corresponding u_i and v_i using knot vectors \mathbf{U}_k and \mathbf{V}_k Compute basis functions N_i and N_j basis functions using u_{span} and v_{span} and knot vectors \mathbf{U}_k and \mathbf{V}_k Compute surface point $\mathbf{S}(u_i, v_j)$ (in $x, y,$ and z directions). Store $u_{span}, v_{span}, N_i, N_j,$ and $\mathbf{S}(u_i, v_j)$ for backward computation **end** **end****end**

Here, u_i (also known as knots) refers to the elements of the knot vector \mathbf{U} (similarly, $v_i \in \mathbf{V}$). The knot vector is a non-decreasing sequence of parametric coordinates, which divide the B-spline into non-uniform piecewise functions. The basis functions N_i^p spans over the parametric domain based on the knot vector and degree as shown in Equation 4 and Equation 5. Note that the formulation explained in Equation 3 uses the vector notation, where \mathbf{P}_{ij} is embedded in \mathfrak{R}^3 .

3.1.2 Surface Point Evaluation

The complete algorithm for forward evaluation of $\mathbf{S}(u, v)$ as described in Piegl and Tiller⁵³ can be divided into three steps:

1. Finding the knot span of $u \in [u_i, u_{i+1})$ and the knot span of $v \in [v_j, v_{j+1})$, where $u_i, u_{i+1} \in \mathbf{U}$ and $v_j, v_{j+1} \in \mathbf{V}$. This is required for the efficient computation of only the non-zero basis functions.
2. Now, we compute the non-zero basis functions $N_i^p(u)$ and $N_j^q(v)$ using the knot span. The basis functions have specific mathematical properties that help us in evaluating them efficiently. The partition of unity and the recursion formula ensures that the basis functions are non-zero only over a finite span of $p + 1$ control points. Therefore, we only compute those $p + 1$ non-zero basis functions instead of the entire n basis function. Similarly in the v direction we only compute $q + 1$ basis functions instead of m .
3. We first compute the weighted control points \mathbf{P}_{ij}^w for a given control point $\mathbf{P}_{ij} = \{\mathbf{P}_x, \mathbf{P}_y, \mathbf{P}_z\}$ and weight w_{ij} as $\{\mathbf{P}_x w, \mathbf{P}_y w, \mathbf{P}_z w\}$ representing the surface after homogeneous transformation for ease of computation. Once the basis functions are computed we multiply the non-zero basis functions with the corresponding weighted control points, \mathbf{P}_{ij}^w . This result, \mathbf{S}' is then used to compute $\mathbf{S}(u, v)$ as $\{S'_x/S'_w, S'_y/S'_w, S'_z/S'_w\}$.

3.1.3 Implementation

In a deep learning system, each layer is considered as an independent unit performing the computation. The layer takes a batch of input during the forward pass and transforms them using the parameters of the layer. Further, in order to reduce the computations needed during the backward pass, we store extra information for computing the gradients during the forward computation. The NURBS layer takes as input the control points, weights, and knot vectors for a batch of NURBS surfaces. We define a parameter to control the number of points evaluated from the NURBS surface. We define a mesh grid of a uniformly spaced set of parametric coordinates $u_{grid} \times v_{grid}$. We perform a parallel evaluation of each surface point $\mathbf{S}(u, v)$ in the $u_{grid} \times v_{grid}$ for all surfaces in the batch and store all the required information for the backward computation. The complete algorithm is explained in Algorithm 1. Our implementation is robust and modular for different applications. For example, if an end-user desires to use this for a B-spline evaluation, they need

to set the knot vectors to be uniform and weights \mathbf{W} to be 1.0. In this case, the forward evaluation can be simplified to $\mathbf{S}(u, v) = \mathbf{f}(\mathbf{P})$. Further, we can also pre-compute the knot spans and basis functions during the initialization of the NURBS layer. During computation, we could make use of tensor comprehension that significantly increases the computational speed. We can also handle NUBS (Non-Uniform B-splines), where the knot vectors are still non-uniform, but the weights W are set to 1.0. Note in the case of B-splines $\Psi = \{\mathbf{P}\}$ (the output from the deep learning framework) and in the case of NUBS $\Psi = \{\mathbf{P}, \mathbf{U}, \mathbf{V}\}$.

3.2 Backward Evaluation for NURBS Surface

In a modular machine learning system, each computational layer requires the gradient of a loss function with respect to the output tensor for the backward computation or the backpropagation. For our NURBS evaluation layer this corresponds to $\partial\mathcal{L}/\partial\mathcal{S}$. As an output to the backward pass, we need to provide $\partial\mathcal{L}/\partial\Psi$. While we represent \mathcal{S} for the boundary surface, computationally, we only compute \mathbf{S} (the set of surface points evaluated from \mathcal{S}). Therefore, we would be using the notation of $\partial\mathbf{S}$ instead of $\partial\mathcal{S}$ to represent the gradients with respect to the boundary surface. Here, we make an assumption that with increasing the number of evaluated points, $\partial\mathbf{S}$ will asymptotically converge to $\partial\mathcal{S}$. Now, we explain the computation of $\partial\mathbf{S}/\partial\Psi$ in order to compute $\partial\mathcal{L}/\partial\Psi$ using the chain rule. In order to explain the implementation of the backward algorithm, we first explain the NURBS derivatives for a given surface point with respect to the different NURBS parameters.

3.2.1 NURBS Derivatives

We rewrite the NURBS formulation as follows:

$$\mathbf{S}(u, v) = \frac{\mathbf{NR}(u, v)}{w(u, v)} \quad (6)$$

where,

$$\begin{aligned} \mathbf{NR}(u, v) &= \sum_{i=0}^n \sum_{j=0}^m N_i^p(u) N_j^q(v) w_{ij} \mathbf{P}_{ij} \\ w(u, v) &= \sum_{i=0}^n \sum_{j=0}^m N_i^p(u) N_j^q(v) w_{ij} \end{aligned}$$

For the forward evaluation of $\mathbf{S}(u, v) = \mathbf{f}(\mathbf{P}, \mathbf{U}, \mathbf{V}, \mathbf{W})$, we can define four derivatives for a given surface evaluation point: $\mathbf{S}_{,u} := \partial\mathbf{S}(u, v)/\partial u$, $\mathbf{S}_{,v} := \partial\mathbf{S}(u, v)/\partial v$, $\mathbf{S}_{,\mathbf{P}} := \partial\mathbf{S}(u, v)/\partial\mathbf{P}$, and $\mathbf{S}_{,\mathbf{W}} := \partial\mathbf{S}(u, v)/\partial\mathbf{W}$. Note that, $\mathbf{S}_{,\mathbf{P}}$ and $\mathbf{S}_{,\mathbf{W}}$ are represent a vector of gradients $\{\mathbf{S}_{,P_{ij}} \forall P_{ij} \in \mathbf{P}\}$ and $\{\mathbf{S}_{,w_{ij}} \forall w_{ij} \in \mathbf{W}\}$. Now, we show the mathematical form of each of these four derivatives. The first derivative is traditionally known as the parametric surface derivative, $\mathbf{S}_{,u}$. Here, $N_{i,u}^p(u)$ refers to the derivative of basis functions with respect to u .

$$\mathbf{S}_{,u}(u, v) = \frac{\mathbf{NR}_{,u}(u, v)w(u, v) - \mathbf{NR}(u, v)w_{,u}(u, v)}{w(u, v)^2} \quad (7)$$

where,

$$\begin{aligned} \mathbf{NR}_{,u}(u, v) &= \sum_{i=0}^n \sum_{j=0}^m N_{i,u}^p(u) N_j^q(v) w_{ij} \mathbf{P}_{ij} \\ w_{,u}(u, v) &= \sum_{i=0}^n \sum_{j=0}^m N_{i,u}^p(u) N_j^q(v) w_{ij} \end{aligned}$$

A similar surface point derivative could be defined for $\mathbf{S}_{,v}$. These derivatives are useful in the sense of differential geometry of NURBS for several CAD applications³³. However, since many deep learning applications such as surface fitting are not dependent on the (u, v) parametric coordinates, we do not use it

in our layer. Also, note that $\mathbf{S}_{,u}$ and $\mathbf{S}_{,v}$ are not the same as $\mathbf{S}_{,\mathbf{U}}$ and $\mathbf{S}_{,\mathbf{V}}$. A discussion about $\mathbf{S}_{,\mathbf{U}}$ and $\mathbf{S}_{,\mathbf{V}}$ is provided later in this section. Now, let us define $\mathbf{S}_{,p_{ij}}(u, v)$.

$$\mathbf{S}_{,p_{ij}}(u, v) = \frac{N_i^p(u)N_j^q(v)w_{ij}}{\sum_{k=0}^n \sum_{l=0}^m N_k^p(u)N_l^q(v)w_{kl}} \quad (8)$$

$\mathbf{S}_{,p_{ij}}(u, v)$ is the rational basis functions themselves. Computing $\mathbf{S}_{,w_{ij}}(u, v)$ is more involved with w_{ij} terms in both the numerator and the denominator of the evaluation.

$$\mathbf{S}_{,w_{ij}}(u, v) = \frac{\mathbf{NR}_{,w_{ij}}(u, v)w(u, v) - \mathbf{NR}(u, v)w_{,w_{ij}}(u, v)}{w(u, v)^2} \quad (9)$$

where,

$$\mathbf{NR}_{,w_{ij}}(u, v) = N_i^p(u)N_j^q(v)\mathbf{P}_{ij}$$

$$w_{,w_{ij}}(u, v) = N_i^p(u)N_j^q(v)$$

3.2.2 Limitations

For the forward evaluation of $\mathbf{S}(u, v) = \mathbf{f}(\mathbf{P}, \mathbf{U}, \mathbf{V}, \mathbf{W})$, we have defined $\mathbf{S}_{,\mathbf{P}}(u, v)$ and $\mathbf{S}_{,\mathbf{W}}(u, v)$ along with the derivatives $\mathbf{S}_{,u}(u, v)$ and $\mathbf{S}_{,v}(u, v)$. However, computing the $\mathbf{S}_{,\mathbf{U}}(u, v)$ and $\mathbf{S}_{,\mathbf{V}}(u, v)$ is not trivial. \mathbf{U} and \mathbf{V} influence the computation of the basis functions. However, due to the recursive computation of the basis functions, computation of these derivatives is not trivial. Further, there is a requirement that the sets \mathbf{U} and \mathbf{V} have to be non-decreasing sequences. Constraining a deep learning network to learn such sequences would be non-trivial. Hence, we set these derivatives to zero. The consequence of this proposition is that \mathbf{U} and \mathbf{V} are not updated during the training process. For this reason, we can set the \mathbf{U} and \mathbf{V} to be fixed non-uniform knot vectors and let the network not predict \mathbf{U} and \mathbf{V} , which simplifies the formulation to $\mathbf{S}(u, v, \mathbf{U}, \mathbf{V}) = \mathbf{f}(\mathbf{P}, \mathbf{W})$. Computing the derivatives with respect to the knot vectors requires significant algorithmic development which we plan to pursue in the future. So, henceforth, we refer to $\mathbf{S}(u, v, \mathbf{U}, \mathbf{V}) = \mathbf{f}(\mathbf{P}, \mathbf{W})$ as the formulation for defining the backward evaluation.

3.2.3 Jacobian for Surface Evaluation

We define the Jacobian for the NURBS evaluation, which is then directly used for the backward evaluation. The Jacobian for each surface evaluation point is represented as the vector $[\mathbf{S}_{,p_{ij}}(u, v) \cdots \mathbf{S}_{,w_{ij}}(u, v) \cdots]$ of length $2 \times n$. However, as noted in the previous section on forward evaluation, the basis functions satisfy the partition of unity and span only $p + 1$ control points starting from u_{span} (correspondingly, $q + 1$ control points starting from v_{span} in the other parametric direction). Therefore, the total number of non-zero elements in a $2nm$ size Jacobian vector is $2(p + 1)(q + 1)$. This Jacobian is for just one surface point evaluation. The Jacobian for the entire surface can be written as follows:

$$J = \begin{pmatrix} \mathbf{B}_1 \\ \mathbf{B}_2 \\ \vdots \\ \mathbf{B}_{n_{grid}m_{grid}} \end{pmatrix} \quad (10)$$

The size of this matrix is $n_{grid}m_{grid} \times 2nm$. Here, \mathbf{B}_r is the Jacobian for one surface point evaluation. As the parametric coordinates keep changing, the position of u_{span} and v_{span} keep changing, and the location of the non-zero elements keeps shifting to form a block diagonal matrix. This Jacobian is $\partial\mathbf{S}/\partial\mathbf{P}$. For completing the backward pass, we multiply $\partial\mathcal{L}/\partial\mathbf{S}$ to $\partial\mathbf{S}/\partial\mathbf{P}$, giving us $\partial\mathcal{L}/\partial\mathbf{P}$. Since, each module in the deep learning framework is independent and modular, we just return this output for the NURBS backward evaluation.

3.2.4 Implementation

For the implementation of the backward pass, since the basis functions are block sparse, we make use of the stored information of u_{span} and v_{span} for identifying the index of the control points derivative and we use the stored basis functions information for computing the Jacobian explained above. This computation is performed for all the surfaces in the batch. This complete algorithm is explained in detail in [Algorithm 2](#).

Algorithm 2: Backward Algorithm

```

Input :  $S'$ 
Output:  $P', W'$ 
Initialize:  $P' \rightarrow 0$ 
Initialize:  $W' \rightarrow 0$ 
for  $k = 1 : surfaces$  do
  for  $j = 1 : m_{grid}$  do
    for  $i = 1 : n_{grid}$  do
      Retrieve  $u_{span}, v_{span}, N_i, N_j, S(u, v)$ 
      for  $r = 0 : p + 1$  do
        for  $h = 0 : q + 1$  do
           $P'_{u_{span}+r, v_{span}+h} = S_{,p_{ij}}(u_i, v_j)$ 
           $W'_{u_{span}+r, v_{span}+h} = S_{,w_{ij}}(u_i, v_j)$ 
        end
      end
    end
  end
end

```

3.3 GPU Implementation

We implemented the code in *Python 3.6*⁵⁵. The backend for the GPU-accelerated code is written in C++ using the Pybind11 API²⁸ and CUDA toolkit⁴⁸ for GPU acceleration and is integrated with PyTorch⁵¹ using a custom layer definition. The forward evaluation can be performed for each surface in the batch for each tuple (u, v) in the meshgrid of $u_{grid} \times v_{grid}$ in parallel. Further, the three coordinates x, y, z are evaluated simultaneously. This enables an embarrassingly parallel implementation on the GPU for the forward evaluation of the NURBS layer. Each $x, y,$ and z component is mapped to a separate thread on the GPU using the 3D block and grid structure in CUDA. In the backward algorithm, the same process is employed with one additional operation. During the backward pass, each surface point gradient needs to be added to several control points that lie in the evaluated point’s span. Hence we perform this operation of the gradient update using a scatter operation by using the indices stored from u_{span} and v_{span} .

4 CAD Applications

The differentiable programming approach explained above is designed mainly for deep learning applications. However, the framework can also be used for some standard CAD operations, such as curve fitting, surface fitting, and surface offsetting. Note that some of these operations could be performed much faster using traditional approaches optimized specifically for each application. However, using our NURBS layer along with gradient-descent-based optimization approaches for these CAD applications is novel and not well explored. Moreover, this shows the versatility of the NURBS layer in handling traditional CAD operations as constraints in a deep learning system.

In order to use our differentiable programming approach for CAD applications, we have to define two key elements: a loss function \mathcal{L} for computing the gradients, and an optimization algorithm. We consider three loss functions: \mathcal{L}_1 loss, \mathcal{L}_2 loss (also called as mean squared error), and the Chamfer distance \mathcal{L}_{CD} . \mathcal{L}_1 loss can be mathematically defined as:

$$\mathcal{L}_1(\mathbf{P}, \mathbf{Q}) = \frac{1}{n_{points}} \left(\sum_{(\mathbf{P}_i, \mathbf{Q}_i) \in (\mathbf{P}, \mathbf{Q})} \|\mathbf{P}_i - \mathbf{Q}_i\|_1 \right) \quad (11)$$

Here, $\|\mathbf{P}_i - \mathbf{Q}_i\|_1$ refers to the L_1 norm of the difference between the two points \mathbf{P}_i and \mathbf{Q}_i . Similarly, we can define \mathcal{L}_2 loss based on the L_2 norm.

$$\mathcal{L}_2(\mathbf{P}, \mathbf{Q}) = \frac{1}{n_{points}} \left(\sum_{(\mathbf{P}_i, \mathbf{Q}_i) \in (\mathbf{P}, \mathbf{Q})} \|\mathbf{P}_i - \mathbf{Q}_i\|_2 \right) \quad (12)$$

While both the \mathcal{L}_1 and \mathcal{L}_2 loss functions are pairwise distance metrics, the Chamfer distance (\mathcal{L}_{CD}) is a global distance metric between two sets of points as shown below.

$$\mathcal{L}_{CD} = \sum_{\mathbf{P}_i \in \mathbf{P}} \min_{\mathbf{Q}_j \in \mathbf{Q}} \|\mathbf{P}_i - \mathbf{Q}_j\|_2 + \sum_{\mathbf{Q}_j \in \mathbf{Q}} \min_{\mathbf{P}_i \in \mathbf{P}} \|\mathbf{P}_i - \mathbf{Q}_j\|_2 \quad (13)$$

For each CAD application, a target point cloud \mathbf{Q} is obtained directly from measurements (for the case of fitting from point clouds) or from analytical computations (for CAD operations such as surface offsetting). While our formulation works well when we initialize the control points and weights to random values (Gaussian distributed), we can also initialize it using a prior enabling faster convergence. After we initialize the control points \mathbf{P} and weights \mathbf{W} , we define the knot vectors \mathbf{U} and \mathbf{V} , which may be non-uniform but are still fixed (non-mutable) in our applications. Now, we can evaluate the surface using \mathbf{P} , \mathbf{W} , \mathbf{U} , and \mathbf{V} . We now evaluate the loss between the evaluated surface \mathbf{S} and \mathbf{Q} using an appropriate loss function \mathcal{L} . We perform an update using gradient descent algorithms and their variants. A simple update for the NURBS parameters can be written as shown in [Equation 14](#).

$$\Psi = \Psi - \alpha \frac{\partial \mathcal{L}}{\partial \Psi} \quad (14)$$

While our formulation can use a simple gradient descent algorithm, in our work, we use more sophisticated algorithms such as stochastic gradient descent (SGD), SGD with momentum, Adam³², and Adagrad⁴⁰. From our experiments illustrated in Appendix, we see that SGD with momentum and Adam perform well in all scenarios and have a fast convergence rate. Now, we discuss the specific CAD applications using our NURBS layer.

4.1 Curve Fitting

We first demonstrate curve fitting using our NURBS layer. In CAD systems, designers often deal with point cloud representations that use coordinate data gathered from data acquisition devices rather than concise parametric equations. In such cases, it is often necessary to employ frameworks that transform the point cloud coordinates into smooth curves that satisfy specific design requirements. While the problem of fitting synthetic splines to point clouds using data-driven techniques has been extensively studied, we explore an unsupervised approach of fitting curves to input points using the NURBS layer discussed in [Section 3](#). We make use of a predefined knot vector in this specific curve fitting example. Hence, to reduce the computation time, we initialize a uniform knot vector \mathbf{U} and compute the non-zero basis functions $N(u)$ and u_{span} as a pre-computation step before evaluating points on the curve.

We demonstrate the results of our layer on 2D and 3D curve fitting of analytical and structured point clouds captured from binary images. We show results for the above-described curves using a different number of control points and evaluation points. We also compare the performance of our layer using \mathcal{L}_1 , \mathcal{L}_2 , and \mathcal{L}_{CD} losses for the analytical curve described in [Figure 3](#). Since our method does not use target control points to fit the curve, some variation in results is expected depending on the number of control points. Our experiments with numerous analytical curves, such as $y = \sin(x) + 2\sin(2x) + \sin(4x)$ as shown in [Figure 3](#) inform us that our layer performs well for variations in both the number of control points and evaluation points with a uniform initialization of control points. The results of the different loss functions are shown

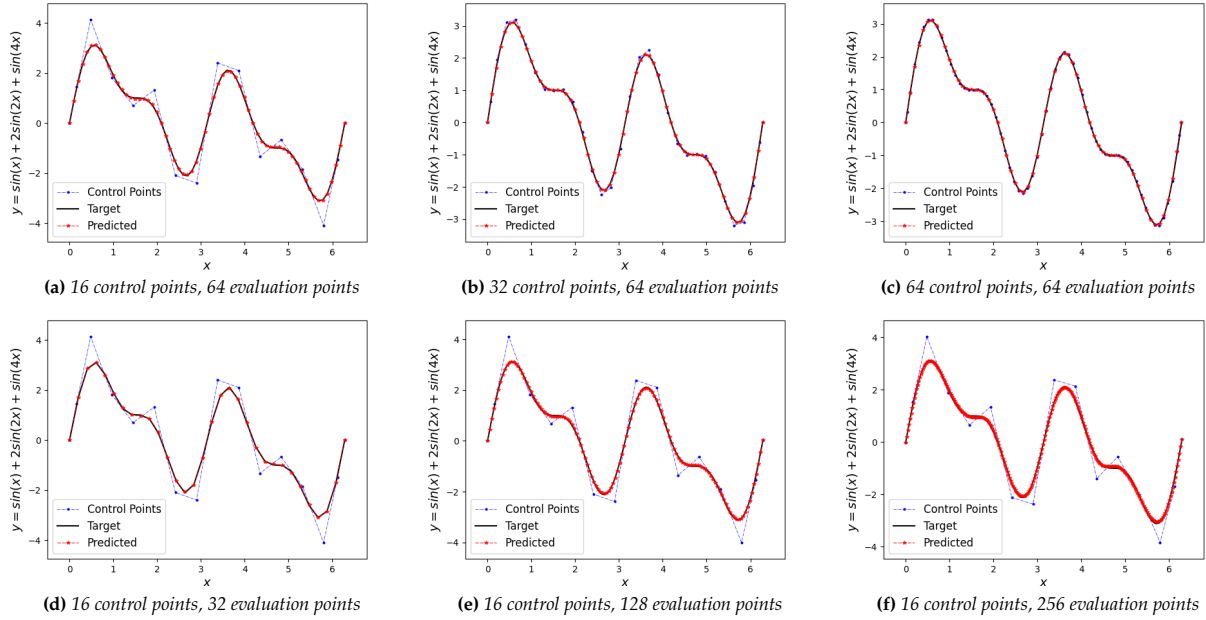


Figure 3: We perform curve fitting for an analytically generated point cloud using the equation of $y = \sin(x) + 2\sin(2x) + \sin(4x)$. We perform this experiment with different number of control points and evaluation points to understand the curve fitting using stochastic gradient descent based algorithms.

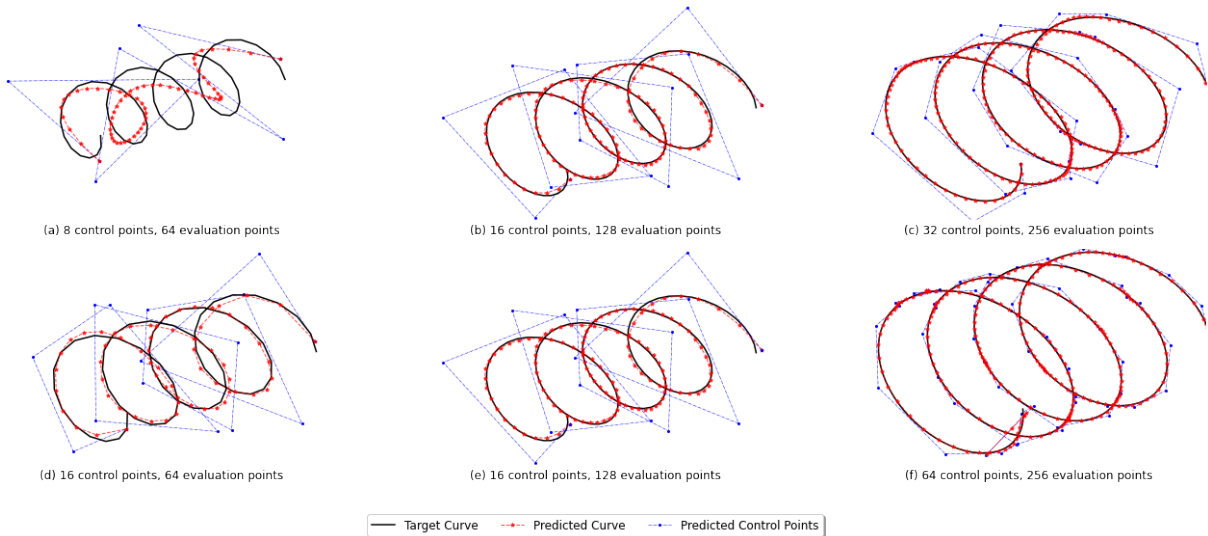


Figure 4: We extend our curve fitting to 3D by performing curve fitting for a 3D helical curve embedded in \mathcal{R}^3 for different number of control points and evaluated points.

in Figure 5 for the curve shown in Figure 4. This shows that the loss function used does not impact the overall quality of the fitted curve. Curve fitting on the 3D helix shown in Figure 4, shows that our layer can generalize for different curve dimensions seamlessly. For higher dimensions, random initializations or initializations from a sampling of the input point cloud outperform uniform initializations for the control points. Figure 4(a) also demonstrates that the fitted curve fails to capture exact curvature details when the number of control points is significantly fewer than what is required for a reasonable approximation of the underlying curve.

Finally, we extend our NURBS layer to a more general curve-fitting problem of random unordered point cloud data. Results of our experiment on the Pixel data provided by Demir et al. ¹⁷ are demonstrated in Figure 6. A point cloud extracted from binary images and random initialization of control points are

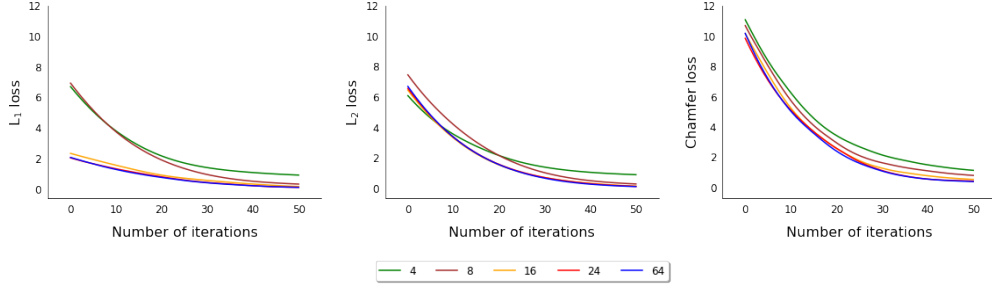


Figure 5: The loss performance with the number of iterations for fitting the 3D helical curve shown in Figure 4. The behavior of the loss is shown for different loss functions and for a variation of number of control points used for the fitting.

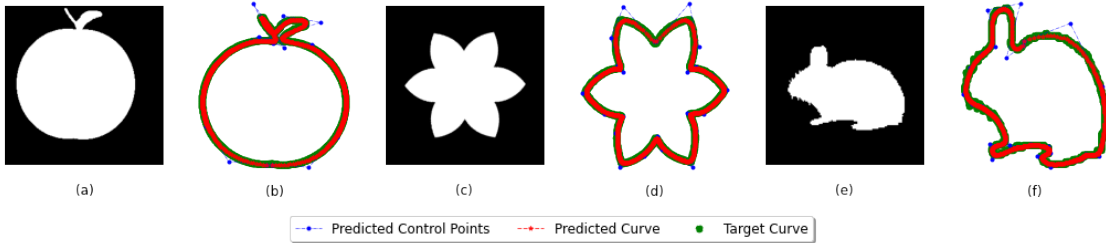


Figure 6: Curve fitting on point cloud data obtained from binary images. We convert the image data into a point cloud using the pixel size and the locations of the pixels. Once we obtain the point clouds, we use curve fitting module with chamfer distance loss function along with regularization to obtain these results.

Table 1: Performance of fitting different curves using the NURBS layer with and without curve length regularization. The Chamfer distance is shown.

Curve	No regularization	Regularization
Analytical	0.0025	0.0016
Helix	0.0370	0.0320
Apple	8.5267	1.6863
Flower	23.2484	0.8383
Bunny	50.0020	1.4099

passed to the NURBS layer. To avoid unnecessary loops and self-intersections in our output curve, we use a curve-length regularization term in addition to the Chamfer distance computed between the target point cloud and predicted curve. As shown in Figure 6 our framework fits the target well for point clouds that are not excessively complex. However, Figure 6(f) demonstrates that complex curves require fine-tuning of the number of control points and curve length regularization parameter to produce perfectly fitted curves. Some complex point cloud data that our framework did not automatically fit well are illustrated in the Appendix. We analyze the performance of our layer for fitting different curves listed under Table 1 using a Chamfer distance loss defined as Equation 13. We set the number of evaluation points for each of these tasks to be twice the number of points in the input point cloud and fix the number of control points to 16 for comparison. Our layer achieves better fitting results when we include a curve length regularization component to our loss function as shown in Table 1. While this difference is less evident for simple analytical curves, the advantage of using a curve length regularization is more pronounced over curves fitted using the Pixel dataset.

4.2 Surface Fitting

The enormous volume of 3D scan data necessitates an efficient pipeline within a CAD systems for the reconstruction of scanned data using NURBS. While several algorithms like least-squares fitting exist to approximate NURBS patches for point cloud data, we extend the experiments of Section 4.1 to surface fitting to illustrate the utility of our layer. We fit both NUBS and NURBS surfaces over unordered point clouds. Similar to Section 4.1, we initialize uniform knot vectors \mathbf{U} and \mathbf{V} in both u and v directions and compute

Table 2: Performance of the different surface CAD applications using the NURBS layer. The Chamfer distance is shown.

Test Case	NUBS	NURBS
Analytical	0.001719	0.001699
Ducky	0.000341	0.000263

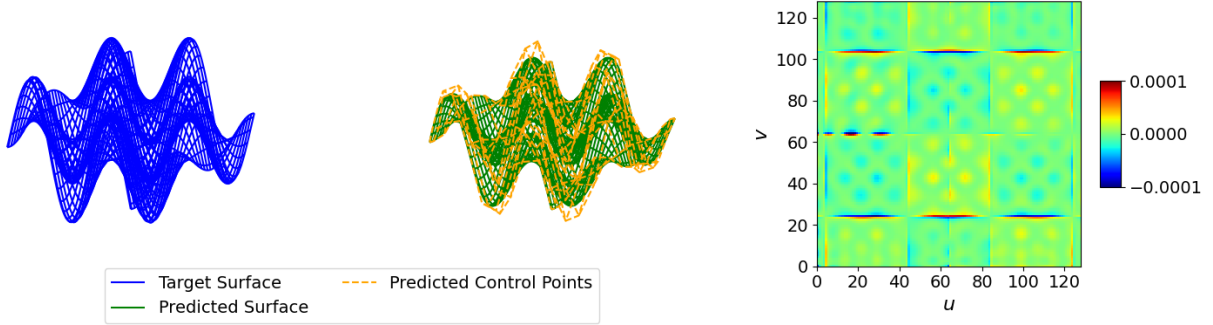


Figure 7: Surface fitting using NURBS for a simple analytical surface represented using $z = \sin(x) * \cos(y)$.

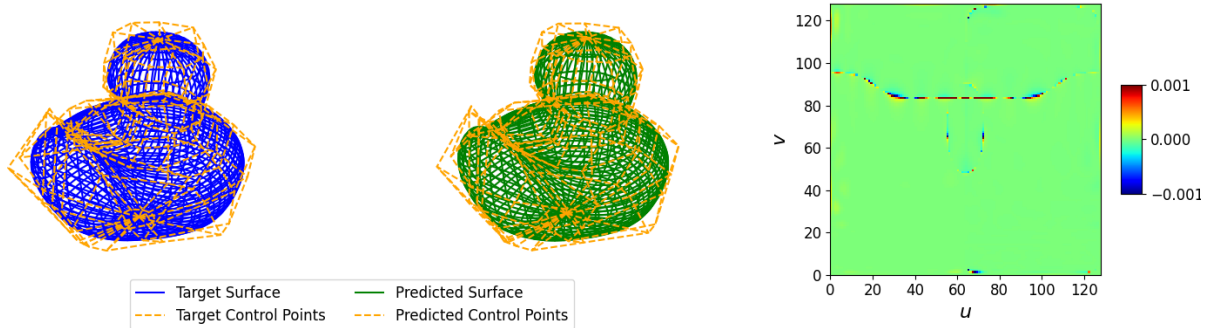


Figure 8: NURBS surface fitting for point cloud representation of Ducky's body.

two dimensional non-zero basis functions $N_i^p(u)$ and $N_j^q(v)$ along with the respective span indices, u_{span} and v_{span} .

In our first example, we test the effectiveness of our layer for fitting a non-rational NUBS surface to the analytical surface defined as $f(x, y) = \sin(x) * \cos(y)$. We randomly initialize a set of control points and set the weights to be 1 (for NUBS). We use \mathcal{L}_2 loss for the comparison between the target surface and the evaluated NUBS surface. As depicted in Figure 7, our layer can generalize well in the 2D parameter space, producing an accurate NUBS representation of the analytical surface. In Figure 7(c), we also visualize the pointwise error (relative error) in the 2D parametric space. We obtain these results for 12 control points in each direction.

In the second example, we show our layer's efficacy in fitting a NURBS surface for the geometry of Ducky shown in Figure 2. We sample points from the Ducky uniformly and then use that as a target for performing a NURBS surface fitting. Since we know the non-uniform knot vectors for the geometry, we use that as a prior for the fixed knot vectors in the NURBS layer and initialize the control points and the weights using random Gaussian distribution. We visualize the final optimized geometry obtained after 1000 iterations in Figure 8. This optimization took less than 2 minutes. In Figure 8 shows the actual target surface and the control points along with the predicted surface with its corresponding control points. The heatmap on the right shows the pointwise relative error between the target surface and the predicted surface in the parametric space. Additional experiments using the Chamfer distance as a loss metric between the input and output are shown in Table 2. As highlighted in the table, our layer evaluates the surface accurately for both NUBS and NURBS cases for both surfaces. This also signifies that multiple sets of control points and weights can give rise to the same NURBS surface.

4.3 Surface Offsetting

Generating an offset surface is one of the fundamental CAD operations. Traditionally an offset surface for NURBS is generated by first performing a Bèzier decomposition of the NURBS surface and performing the offset for each patch. However, this changes the parameterization of the resulting offset surfaces. However, specific applications might require an offset surface with the same parameterization. We can easily use our NURBS layer to perform such an offset operation. Note that this approach only works for reasonable offset distances such that the topology of the offset surface does not change.

To perform the offset operation, we first compute a dense set of points and normals at specific (u, v) , and calculate the points on the corresponding offset surface by moving the points along the normal by the offset distance. We then fit a NURBS surface for the offset point cloud data using the same parameterization of the base surface using the surface fitting method (see Section 4.2).

Using our offsetting method, we can also generate offsets of objects consisting of multiple NURBS surfaces. Generating offset surfaces from multiple base surfaces requires applying constraints on the control points on the common edges of the base surfaces. While computing the surface normals, we identify the surface points that are along the shared edge. We then compute the average normals of these common points and then normalize them. Calculating the average normal allows us to ensure the continuity of the offset point cloud data (see Figure 13 for additional details). We then apply the constraints on the control points of the common edges to be the same on both the surfaces that share the common edge. To ensure this continuity for the NURBS surfaces, we create a list of the shared control points. After the surface fitting iteration, the control points are updated; based on the shared list, i.e. the control points of the common edge are assigned the same coordinates. We perform this by computing the average of all the common points and setting them to be the same on both surfaces.

Figure 9 shows examples of the surface offsets generated using our NURBS layer. Figure 9(a) is a single surface patch with a double-curved surface. Figure 9(b) is a set of C^0 continuous surfaces with a single shared edge. Figure 9(c) is a set of C^1 continuous conic section surfaces. Figure 9(d) is a set of surfaces from a wind turbine blade model. To compare the accuracy of our NURBS layer approach for offset surfaces, we computed a simpler offset by offsetting the control points along the average normal direction of the control mesh. This approach works well for surfaces with low curvature. We then evaluated the computed offset surface at $25\times$ denser points than the number of points used for fitting and computed the Chamfer distance with the input offset points. We find that our fitting approach achieves a lower Chamfer distance than the control point offset approach for all cases, as seen in Table 3.

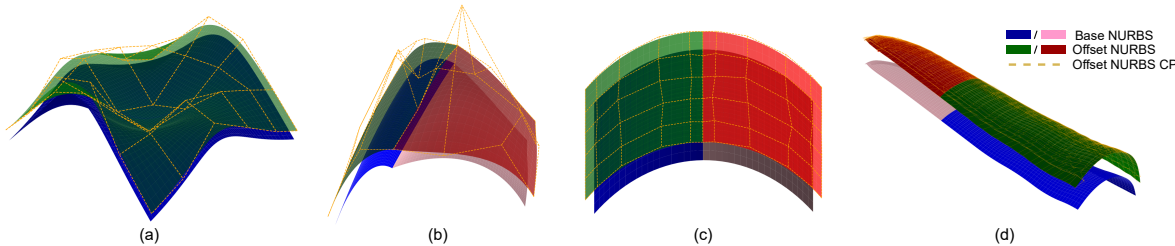


Figure 9: Test cases for NURBS surface offset (a) Double curved surface, (b) C^0 continuous multi patch, (c) C^1 continuous multi patch, and (d) C^1 continuous patches of the aerofoil profile of a wind turbine blade.

Table 3: Normalized Chamfer distance between the offset surface and the offset point cloud using our NURBS layer and SGD compared to direct offset of the control points (CP Offset). The Chamfer distance is normalized using the minimum size of the bounding box of the base surface along the offset direction.

Test Case	Min BB Size	Offset Distance	NURBS Layer Offset CD	CP Offset CD
Double Curve	11.54	1.50	0.023489	0.023951
Multi patch - C^0	0.75	0.10	0.000649	0.000823
Multi patch - C^1	6.32	2.00	0.038936	0.039039
Aerofoil Surface	0.66	0.25	0.052927	0.054461

5 Deep Learning Applications

In the previous section, we saw the NURBS layer used for several CAD operations. In this section, we will show the utility of our NURBS layer to general deep learning applications. We test the utility of the NURBS layer in two deep learning frameworks. The first framework is supervised NURBS reconstruction of point cloud data based on Sharma et al. ⁶⁰. The second framework is a NURBS-based shell analysis of heart valve data based on Balu et al. ⁵. The data sets for both these frameworks are available online. We replaced the spline implementation in these layers with our NURBS layer. We will discuss the integration of the NURBS layer in both these frameworks below.

5.1 Point Cloud Reconstruction

The 3D spatial data obtained from geometric acquisition devices are low-level point cloud representations that offer limited structural information about the underlying geometry. To ease the integration of deep learning with CAD pipelines, recent works on point cloud reconstruction have tried fitting different parametric primitives over the input data. In this direction, Sharma et al. ⁶⁰ have introduced an end-to-end trainable network called ParSeNet that fits an assembly of geometric primitives, including B-spline patches, to a segmented point cloud. We integrated our NURBS layer with the ParSeNet framework by replacing their B-spline fitting with NURBS.

The ParSeNet architecture is divided into three stages. The first stage incorporates prior work done in point cloud segmentation ⁵⁴ to decompose the input point cloud into segments classified under a parametric patch type. The second stage is the spline fitting SplineNet that generates B-spline patches to the segmented point cloud data. The final stage performs geometric optimizations to seamlessly stitch the collection of predicted primitives together into a single object. We are interested in replacing the surface evaluation performed in the SplineNet stage of their network with our NURBS layer for the experiments in this section. For training and testing our experiments, we use the SplineDataset provided by Sharma et al. ⁶⁰. The SplineDataset is a diverse collection of open and closed splines that have been extracted from one million CAD geometries included in the ABC dataset. We run our experiments on open splines that are split into 3.2K, 3K, and 3K for training, testing, and validation.

Table 4: Ablation study for SplineNet results. We perform several experiments and compute the control point regression (CP) loss, patch distance (PD) loss, Laplacian loss and total loss.

Experiment	CP loss	PD loss	Laplacian loss	Total loss
SplineNet	0.0038	0.0174	0.0003	0.0052
SplineNet with NURBS layer	0.0048	0.0184	0.0003	0.0062
Rational B-splines 0.1 weight PD loss	0.0045	0.0722	0.0004	0.0114
Rational B-splines 1.0 weight PD loss	0.0045	0.0178	0.0004	0.0059
Rational B-splines 10.0 weight PD loss	0.0064	0.0143	0.0009	0.0073

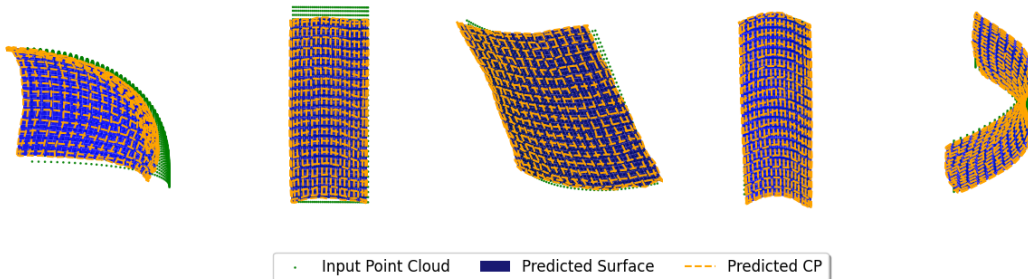


Figure 10: Point clouds and reconstructed B-spline surfaces (40×40) produced by SplineNet where the spline evaluation is replaced with our NURBS layer.

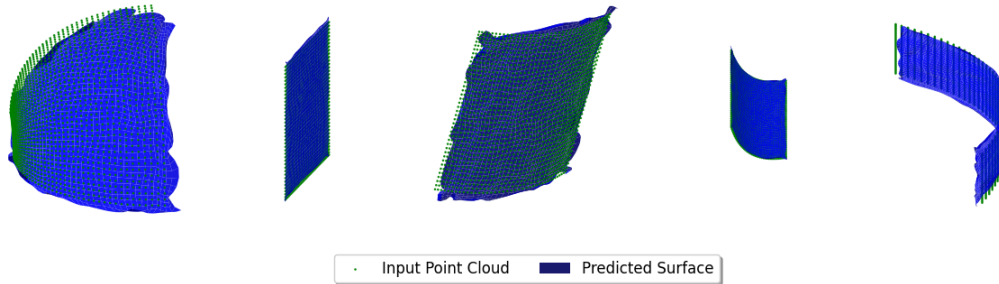


Figure 11: Point clouds and reconstructed rational B-spline surfaces (40×40) produced by SplineNet modified to accommodate rational (non-unity) control point weights.

In our work, we use the same SplineNet architecture for generating the control points to illustrate the usefulness of our NURBS layer in generalizing the B-spline patches predicted from their network to rational B-splines and NURBS surfaces. We generalize the surface evaluation to compute the Patch distance loss to incorporate rational B-splines and NURBS surfaces. We evaluate the results obtained by integrating our layer using three losses: control point regression loss, Laplacian loss, and patch distance loss⁶⁰. The results obtained for the various losses are illustrated in Table 4. We also visualize a few anecdotal predicted surfaces along with the input point cloud in Figure 10 and Figure 11.

5.2 Deep Learning for Valve Analysis

Analysis of bioprosthetic heart valves is essential for obtaining diagnostic information such as estimating the remaining life, fatigue, and patient-specific design. Traditionally, analysis of deformation behavior is performed using finite element or isogeometric analysis. However, such analyses are often computationally intensive. Recently, Balu et al.⁵ proposed a deep learning framework for performing finite element analysis (DLFEA) using a NURBS-aware convolutional neural network. Each heart valve is represented using three NURBS surface patches, and isogeometric analysis is performed to obtain the deformations for each control point under constant pressure applied during the valve closure. Fixed boundary conditions are applied on the valve edges that will be sutured to the aorta. In their work, they generate a large dataset of input geometry, pressure, thickness, and corresponding target deformations of the control points. However, their work does not perform a NURBS surface reconstruction loss for obtaining the deformations, which are more physically meaningful. Further, they did not explore the application of the fixed boundary conditions in their work. This was implicitly enforced in their work by modifying the loss function.

In this work, we use the dataset available from their work to demonstrate the utility of our NURBS layer in performing an evaluation of the deformations for the leaflets of the bioprosthetic heart valve. We perform a comparison between DLFEA, DLFEA with additional surface reconstruction loss (DLFEA-SR), and DLFEA with additional surface reconstruction loss and boundary condition enforcement loss (DLFEA-BC). In Table 5, we show the results obtained on a test dataset (not used during the training). The CP loss is the

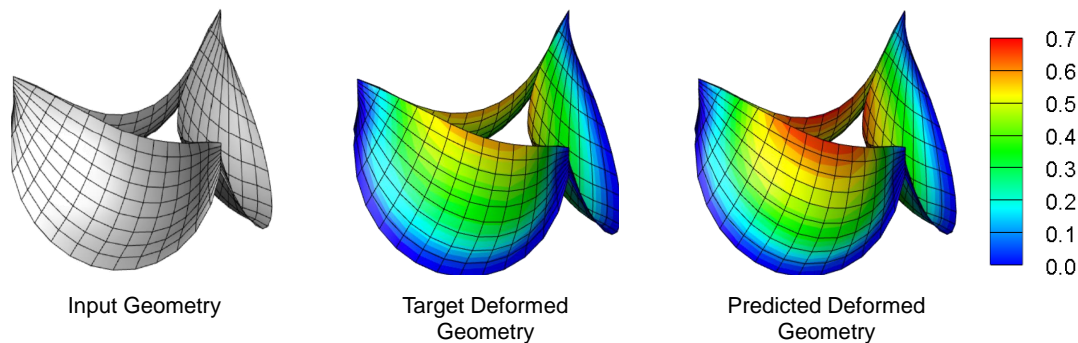


Figure 12: Visualization of an anecdotal bioprosthetic heart valve for DLFEA from the test dataset. We show the input geometry along with the target deformed geometry along and the predicted deformed geometry.

Table 5: Performance comparison of DLFEA, DLFEA-SR and DLFEA-BC. The metrics compared is the error on the test dataset for control points reconstruction, NURBS surface reconstruction, and boundary condition enforcement.

Test Case	CP loss	SR loss	BC loss
DLFEA	0.007795	0.004472	37.692390
DLFEA-SR	0.012845	0.004758	46.137878
DLFEA-BC	0.012830	0.005686	10.901491

\mathcal{L}_2 loss between the input control points and the target control points, whereas the SR loss represents the \mathcal{L}_2 loss between the NURBS surface reconstruction of the target deformed shape and the actual deformed shape. We observe that DLFEA performs very well for the CP loss (naturally because it was originally trained using that) but does not do well on the BC loss. The DLFEA-SR performs comparably for SR loss but has worse performance for BC loss. At the same time, DLFEA-BC performs the best for BC loss while performing comparably (although worse) on CP loss and SR loss. While the DLFEA-BC performs worse, the enforcement of boundary conditions makes it more physically meaningful. Further, in this ablation study, we show the result for each loss function applied independently. In general, we use a combined loss with several loss functions in tandem as done in Section 5.1. Finally, we show the visualization of DLFEA-BC along with the input geometry, the target deformed geometry, and the predicted deformed geometry in Figure 12.

6 Conclusions

We have developed a differentiable NURBS layer that can be directly integrated with existing machine learning frameworks. We have developed the mathematical framework that enables both forward evaluation and backpropagation of the losses while training. Our layer is GPU-accelerated to allow fast evaluation of NURBS surface points and fast backpropagation of the derivatives. We have demonstrated the utility of our NURBS layer for several CAD applications as well as deep learning applications. Our NURBS layer performs at the same level as existing standalone spline solutions used previously in the literature. Future work on the NURBS layer includes developing support for trimmed NURBS surfaces and integrating complex curve constraints along trim edges for the watertight representation of CAD models. We plan to release the code for our NURBS layer open-source along with this paper. We believe this NURBS layer will be the first step to better integrate deep learning with CAD and lead to more diverse machine learning CAD applications.

References

- [1] Alnæs, M., Blechta, J., Hake, J., Johansson, A., Kehlet, B., Logg, A., Richardson, C., Ring, J., Rognes, M.E., Wells, G.N., 2015. The FEniCS project version 1.5. Archive of Numerical Software 3.
- [2] Attene, M., Patanè, G., 2010. Hierarchical structure recovery of point-sampled surfaces. Computer Graphics Forum 29.
- [3] Atzmon, M., Lipman, Y., 2020. Sal: Sign agnostic learning of shapes from raw data, in: Proceedings of the IEEE/CVF Conference on Computer Vision and Pattern Recognition, pp. 2565–2574.
- [4] Balestrieri, R., et al., 2018. A spline theory of deep learning, in: International Conference on Machine Learning, PMLR. pp. 374–383.
- [5] Balu, A., Nallagonda, S., Xu, F., Krishnamurthy, A., Hsu, M.C., Sarkar, S., 2019. A deep learning framework for design and analysis of surgical bioprosthetic heart valves. Scientific Reports 9, 1–12.
- [6] Barill, G., Dickson, N.G., Schmidt, R., Levin, D.I., Jacobson, A., 2018. Fast winding numbers for soups and clouds. ACM Transactions on Graphics 37, 1–12.
- [7] Baydin, A.G., Pearlmutter, B.A., Radul, A.A., Siskind, J.M., 2018. Automatic differentiation in machine learning: a survey. [arXiv:1502.05767](https://arxiv.org/abs/1502.05767).
- [8] Blondel, M., Teboul, O., Berthet, Q., Djolonga, J., 2020a. Fast differentiable sorting and ranking. ArXiv abs/2002.08871.

- [9] Blondel, M., Teboul, O., Berthet, Q., Djolonga, J., 2020b. Fast differentiable sorting and ranking. [arXiv:2002.08871](https://arxiv.org/abs/2002.08871).
- [10] Chen, W., Ling, H., Gao, J., Smith, E., Lehtinen, J., Jacobson, A., Fidler, S., 2019. Learning to predict 3D objects with an interpolation-based differentiable renderer, in: *Advances in Neural Information Processing Systems*, pp. 1–11.
- [11] Chen, Z., Tagliasacchi, A., Zhang, H., 2020. BSP-Net: Generating compact meshes via binary space partitioning, in: *Conference on Computer Vision and Pattern Recognition*, pp. 45–54.
- [12] Cho, M., Joshi, A., Lee, X.Y., Balu, A., Krishnamurthy, A., Ganapathysubramanian, B., Sarkar, S., Hegde, C., . Differentiable programming for piecewise polynomial functions, in: *Association for the Advancement of Artificial Intelligence Conference*, pp. 1–10.
- [13] Choy, C.B., Xu, D., Gwak, J., Chen, K., Savarese, S., 2016. 3D-R2N2: A unified approach for single and multi-view 3D object reconstruction. [arXiv:1604.00449](https://arxiv.org/abs/1604.00449).
- [14] Cuturi, M., Teboul, O., Vert, J.P., 2019. Differentiable ranks and sorting using optimal transport. [arXiv:1905.11885](https://arxiv.org/abs/1905.11885).
- [15] Davies, T., Nowrouzezahrai, D., Jacobson, A., 2020. Overfit neural networks as a compact shape representation. [arXiv:2009.09808](https://arxiv.org/abs/2009.09808).
- [16] Degraeve, J., Hermans, M., Dambre, J., Wyffels, F., 2017. A differentiable physics engine for deep learning in robotics. *Frontiers Neurorobotics* 13.
- [17] Demir, I., Hahn, C., Leonard, K., Morin, G., Rahbani, D., Panotopoulou, A., Fondevilla, A., Balashova, E., Durix, B., Kortylewski, A., 2019. Skelneton 2019: Dataset and challenge on deep learning for geometric shape understanding. [arXiv:1903.09233](https://arxiv.org/abs/1903.09233).
- [18] Deng, B., Genova, K., Yazdani, S., Bouaziz, S., Hinton, G., Tagliasacchi, A., 2020. CvxNet: Learnable convex decomposition, in: *Conference on Computer Vision and Pattern Recognition*, pp. 31–44.
- [19] Deng, C., Lin, H., 2014. Progressive and iterative approximation for least squares B-spline curve and surface fitting. *Computer-Aided Design* 47, 32–44.
- [20] Djolonga, J., Krause, A., 2017. Differentiable learning of submodular models, in: *Neural Information Processing Systems*, p. 1014–1024.
- [21] Duda, R.O., Hart, P.E., 1972. Use of the Hough transformation to detect lines and curves in pictures. *Communications of the ACM* 15, 11–15.
- [22] Erwinski, K., Paprocki, M., Wawrzak, A., Grzesiak, L.M., 2016. Neural network contour error predictor in CNC control systems, in: *2016 21st International Conference on Methods and Models in Automation and Robotics (MMAR)*, IEEE. pp. 537–542.
- [23] Fey, M., Lenssen, J.E., Weichert, F., Müller, H., 2018. SplineCNN: Fast geometric deep learning with continuous B-spline kernels, in: *Conference on Computer Vision and Pattern Recognition*, pp. 869–877.
- [24] Girdhar, R., Fouhey, D.F., Rodriguez, M., Gupta, A., 2016. Learning a predictable and generative vector representation for objects. [arXiv:1603.08637](https://arxiv.org/abs/1603.08637).
- [25] Groueix, T., Fisher, M., Kim, V.G., Russell, B.C., Aubry, M., 2018. AtlasNet: A Papier-Mâché approach to learning 3D surface generation. [arXiv:1802.05384](https://arxiv.org/abs/1802.05384).
- [26] Innes, M., Edelman, A., Fischer, K., Rackauckas, C., Saba, E., Shah, V.B., Tebbutt, W., 2019. A differentiable programming system to bridge machine learning and scientific computing. [ArXiv abs/1907.07587](https://arxiv.org/abs/1907.07587).
- [27] Innes, M.J., 2020. Algorithmic differentiation, in: *Machine Learning and Systems*, pp. 1–12.
- [28] Jakob, W., Rhinelander, J., Moldovan, D., 2017. Pybind11 - Seamless operability between C++ 11 and Python.

- [29] Johnston, A., Garg, R., Carneiro, G., Reid, I., van den Hengel, A., 2017. Scaling CNNs for high resolution volumetric reconstruction from a single image, in: 2017 IEEE International Conference on Computer Vision Workshops (ICCVW), pp. 930–939.
- [30] Joshi, A., Cho, M., Shah, V., Pokuri, B., Sarkar, S., Ganapathysubramanian, B., Hegde, C., 2020. InvNet: Encoding geometric and statistical invariances in deep generative models, in: Association for the Advancement of Artificial Intelligence Conference, pp. 1–8.
- [31] Kaiser, A., Zepeda, J.A.Y., Boubekur, T., 2019. A survey of simple geometric primitives detection methods for captured 3D data. *Computer Graphics Forum* 38, 167–196.
- [32] Kingma, D.P., Ba, J., 2014. Adam: A method for stochastic optimization. arXiv preprint arXiv:1412.6980 .
- [33] Krishnamurthy, A., Khardekar, R., McMains, S., Haller, K., Elber, G., 2009. Performing efficient NURBS modeling operations on the GPU. *IEEE Transactions on Visualization and Computer Graphics* 15, 530–543.
- [34] Li, L., Sung, M., Dubrovina, A., Yi, L., Guibas, L.J., 2019. Supervised fitting of geometric primitives to 3D point clouds. *Conference on Computer Vision and Pattern Recognition (CVPR)* .
- [35] Li, T.M., Aittala, M., Durand, F., Lehtinen, J., 2018a. Differentiable Monte-Carlo ray tracing through edge sampling. *ACM Trans. Graphic.* 37, 1–11.
- [36] Li, T.M., Gharbi, M., Adams, A., Durand, F., Ragan-Kelley, J., 2018b. Differentiable programming for image processing and deep learning in halide. *ACM Trans. Graphic.* 37, 1–13.
- [37] Li, Y., Wu, X., Chrysathou, Y., Sharf, A., Cohen-Or, D., Mitra, N.J., 2011. GlobFit: Consistently fitting primitives by discovering global relations. *ACM Transactions on Graphics* 30.
- [38] Lin, H., Wang, G., Dong, C., 2004. Constructing iterative non-uniform B-spline curve and surface to fit data points. *Science in China Series: Information Sciences* 47, 315–331.
- [39] Lin, H.W., Bao, H.J., Wang, G.J., 2005. Totally positive bases and progressive iteration approximation. *Computers & Mathematics with Applications* 50, 575–586.
- [40] Lydia, A., Francis, S., 2019. Adagrad-An optimizer for stochastic gradient descent. *Int. Journal of Computing and Information Sciences* 6.
- [41] Macqueen, J., 1967. Some methods for classification and analysis of multivariate observations, in: In 5th Berkeley Symposium on Mathematical Statistics and Probability, pp. 281–297.
- [42] Mescheder, L., Oechsle, M., Niemeyer, M., Nowozin, S., Geiger, A., 2019. Occupancy networks: Learning 3D reconstruction in function space, in: *Conference on Computer Vision and Pattern Recognition*, pp. 4460–4470.
- [43] Min, K., Lee, C.H., Yan, C., Fan, W., Hu, P., 2020. Six-dimensional b-spline fitting method for five-axis tool paths. *The International Journal of Advanced Manufacturing Technology* , 1–14.
- [44] Minto, L., Zanuttigh, P., Pagnutti, G., 2018. Deep learning for 3D shape classification based on volumetric density and surface approximation clues., in: *VISIGRAPP (5: VISAPP)*, pp. 317–324.
- [45] Mo, K., Guerrero, P., Yi, L., Su, H., Wonka, P., Mitra, N.J., Guibas, L.J., 2019. StructureNet: Hierarchical graph networks for 3D shape generation. ArXiv [arXiv:1908.00575](https://arxiv.org/abs/1908.00575).
- [46] Mykhaskiv, O., Banović, M., Auriemma, S., Mohanamurthy, P., Walther, A., Legrand, H., Müller, J.D., 2018. NURBS-based and parametric-based shape optimization with differentiated CAD kernel. *Computer-Aided Design and Applications* 15, 916–926.
- [47] Niemeyer, M., Mescheder, L., Oechsle, M., Geiger, A., 2020. Differentiable volumetric rendering: Learning implicit 3D representations without 3D supervision, in: *Conference on Computer Vision and Pattern Recognition*, pp. 3504–3515.

- [48] NVIDIA, 2011. NVIDIA CUDA C programming guide. NVIDIA Corporation 120, 8.
- [49] Pagnutti, G., Zanuttigh, P., 2015. Scene segmentation based on NURBS surface fitting metrics, in: Smart Tools and Apps for Graphics - Eurographics Italian Chapter Conference, pp. 1–10.
- [50] Park, J.J., Florence, P., Straub, J., Newcombe, R., Lovegrove, S., 2019. DeepSDF: Learning continuous signed distance functions for shape representation, in: Computer Vision and Pattern Recognition, pp. 165–174.
- [51] Paszke, A., Gross, S., Massa, F., Lerer, A., Bradbury, J., Chanan, G., Killeen, T., Lin, Z., Gimelshein, N., Antiga, L., et al., 2019. PyTorch: An imperative style, high-performance deep learning library. [arXiv:1912.01703](https://arxiv.org/abs/1912.01703).
- [52] Peng, S., Niemeyer, M., Mescheder, L., Pollefeys, M., Geiger, A., 2020. Convolutional occupancy networks. [arXiv preprint arXiv:2003.04618](https://arxiv.org/abs/2003.04618) 2.
- [53] Piegl, L., Tiller, W., 1997. The NURBS Book (2nd Ed.). Springer-Verlag, Berlin, Heidelberg.
- [54] Qi, C.R., Su, H., Mo, K., Guibas, L.J., 2017. Pointnet: Deep learning on point sets for 3D classification and segmentation. [arXiv:1612.00593](https://arxiv.org/abs/1612.00593).
- [55] Rossum, G., 1995. Python Reference Manual. Technical Report. CWI (Centre for Mathematics and Computer Science). Amsterdam, The Netherlands, The Netherlands.
- [56] Salas-Moreno, R.F., Glocken, B., Kelly, P.H.J., Davison, A.J., 2014. Dense planar SLAM, in: 2014 IEEE International Symposium on Mixed and Augmented Reality (ISMAR), pp. 157–164.
- [57] Schafer, F., Kloc, M., Bruder, C., Lorch, N., 2020. A differentiable programming method for quantum control. [ArXiv](https://arxiv.org/abs/2003.04618) .
- [58] Schnabel, R., Wahl, R., Klein, R., 2007. Efficient ransac for point-cloud shape detection. *Computer Graphics Forum* 26, 214–226.
- [59] Sharma, G., Goyal, R., Liu, D., Kalogerakis, E., Maji, S., 2018. CSGNet: Neural shape parser for constructive solid geometry. [arXiv:1712.08290](https://arxiv.org/abs/1712.08290).
- [60] Sharma, G., Liu, D., Maji, S., Kalogerakis, E., Chaudhuri, S., Měch, R., 2020. ParSeNet: A parametric surface fitting network for 3D point clouds. [arXiv:2003.12181](https://arxiv.org/abs/2003.12181).
- [61] Shen, C.H., Huang, S.S., Fu, H., Hu, S.M., 2011. Adaptive partitioning of urban facades. *ACM Transactions on Graphics* 30, 184:1–184:9.
- [62] Shen, Y., Feng, C., Yang, Y., Tian, D., 2017. Neighbors do help: Deeply exploiting local structures of point clouds. [ArXiv abs/1712.06760](https://arxiv.org/abs/1712.06760).
- [63] Sherifdeen, S., Ragusa, J.C., Morel, J.E., Adams, M.L., Bui-Thanh, T., 2019. Accelerating PDE-constrained inverse solutions with deep learning and reduced order models. [arXiv:1912.08864](https://arxiv.org/abs/1912.08864).
- [64] Tatarchenko, M., Dosovitskiy, A., Brox, T., 2017. Octree generating networks: Efficient convolutional architectures for high-resolution 3D outputs. [arXiv:1703.09438](https://arxiv.org/abs/1703.09438).
- [65] Tulsiani, S., Su, H., Guibas, L.J., Efros, A.A., Malik, J., 2016. Learning shape abstractions by assembling volumetric primitives. [ArXiv abs/1612.00404](https://arxiv.org/abs/1612.00404). [arXiv:1612.00404](https://arxiv.org/abs/1612.00404).
- [66] Ugolotti, M., Vaughan, B., Orkwis, P.D., 2021. Differentiated ml-based modeling of structured grids for gradient-based optimization, in: AIAA Scitech 2021 Forum, p. 0895.
- [67] Vlastelica, M., Paulus, A., Musil, V., Martius, G., Rolínek, M., 2020. Differentiation of blackbox combinatorial solvers. [arXiv:1912.02175](https://arxiv.org/abs/1912.02175).
- [68] Wang, P.S., Liu, Y., Guo, Y.X., Sun, C.Y., Tong, X., 2017. O-CNN. *ACM Transactions on Graphics* 36, 1–11.

- [69] Wang, Y., Sun, Y., Liu, Z., Sarma, S.E., Bronstein, M.M., Solomon, J.M., 2018. Dynamic graph CNN for learning on point clouds. ArXiv abs/1801.07829. [arXiv:1801.07829](#).
- [70] Wu, Z., Song, S., Khosla, A., Yu, F., Zhang, L., Tang, X., Xiao, J., 2015. 3D ShapeNets: A deep representation for volumetric shapes. [arXiv:1406.5670](#).
- [71] Yu, L., Li, X., Fu, C., Cohen-Or, D., Heng, P., 2018. EC-Net: An edge-aware point set consolidation network. ArXiv [arXiv:1807.06010](#).
- [72] Zhang, X., 2018. CAD-based geometry parametrisation for shape optimisation using Non-uniform Rational B-splines. Ph.D. thesis. Queen Mary University of London.

Appendix

A Test Surface Details

Table 6 shows geometrical details for each surface that was used for the fitting and surface offset tests. The surface fitting examples (Analytical and Ducky) are evaluated at 128^2 and 512^2 points, respectively. The surface offset test examples are evaluated at 20^2 points each.

Table 6: NURBS parameters for the surface fitting and surface offset test examples.

Surface Model	p	q	n	m
Analytical	3	3	12	12
Ducky	3	3	14	13
Double Curve	3	3	6	6
Multi Patch - C^0	3	3	4	4
Multi Patch - C^1	3	3	6	6
Aerofoil	3	3	50	24

B Computing Normals on the Common Edge

For C^0 continuous surfaces, the surface normals at the common edge of two surfaces point in different directions. Hence, if the individual surface normals are used for the offset operation, it might lead to a gap or self-intersection between the offset surfaces. To deal with this case, we identify the common control points at the surface edges, and we recompute the resulting normal as the average of both the individual surface normals as shown in **Figure 13**. We then use this average normal to move the points on the common edges to generate the offset points.

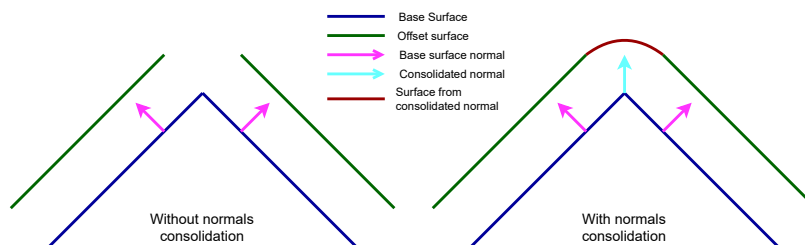


Figure 13: Absence of normals consolidation may produce discontinuous surfaces especially for C^0 connectivity (shown on left). Normals consolidation ensures connectivity for the offset surfaces (shown of right).

C Additional Curve Fitting Results

We tested the curve fitting example of the 3D helix shown in Figure 4 with different optimizers. Figure 14 shows the results for four different optimizers used in this test. It can be seen that all the optimizers converge to the same value for the \mathcal{L}_2 loss, but the Adagrad optimizer converges to a different value for the \mathcal{L}_1 and \mathcal{L}_{CD} loss. In addition, it can be seen that SGD with momentum has the fastest convergence rates for all losses.

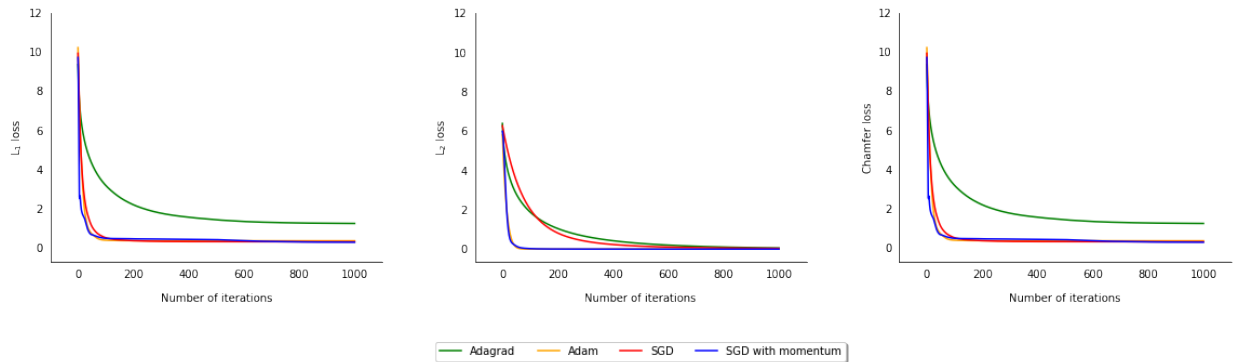


Figure 14: Results of the curve fitting on a 3D helix point data with different optimizer.

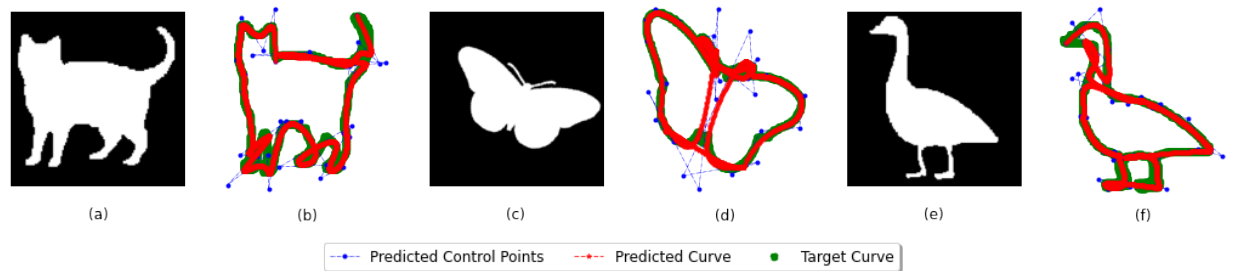


Figure 15: Curve fitting test performed on various skeleton geometry which results in an invalid curve generation due to self-intersecting geometry.

For some complex shapes, our method is not able to generate a curve without self-intersections and loops for the Pixel dataset. This is because the weightage of the curve length regularization parameter needs to be tuned for each object based on its complexity. Figure 15 shows the results from 3 curve fitting tests where the curves generated are self-intersecting. Adding additional constraints to prevent this is a possible future research direction.